Geophysical Research Letters

RESEARCH LETTER
10.1002/2018GL077413

Special Section:
New understanding of the solar eclipse effects on geospace: The 21 August 2017 Solar Eclipse

Vertical and Oblique Ionosphere Sounding During the 21 August 2017 Solar Eclipse

Terence Bullett[1,2] **and Justin Mabie**[1,2]

[1]Cooperative Institute for Research in Environmental Sciences, University of Colorado Boulder, Boulder, CO, USA, [2]National Centers for Environmental Information, National Oceanic and Atmospheric Administration, Boulder, CO, USA

Abstract On 21 August 2017, a total solar eclipse crossed North America. Two Vertical Incident Pulsed Ionospheric Radar ionosondes were operated, one deployed under totality at Lusk, Wyoming, and another south of totality, 313 km away from the geomagnetic meridian in Boulder, Colorado. The two Vertical Incident Pulsed Ionospheric Radar systems were synchronized for precise observation of both vertical and oblique group and phase paths. Hand-scaled values of virtual heights and critical frequencies are presented. Arrival angles were computed using phase interferometry and used to compute equivalent vertical critical frequencies at the oblique midpoint. Oblique propagation geometry and horizontal gradients allowed measurement of *F*2 layer during ionosphere *G* condition where foF1 exceed foF2 after totality.

Plain Language Summary This paper presents the initial results of an experiment to measure the effect on the Earth's ionosphere of the North American 21 August 2017 total solar eclipse. The ionosphere is created by solar radiation and the sudden disappearance of this energy is an opportunity to study how the ionosphere behaves under these conditions. Unique to this experiment was the ability to have two highly advanced high-frequency radars, or ionosondes, with one deployed into the totality region in Wyoming and another just outside totality in Colorado, operating from 1.5 to 12 MHz radio frequency. These instruments reflect radio waves off of the ionosphere to measure its height and density. The radars were synchronized to provide rapid measurements both overhead and between the two instrument locations. High time resolution data were manually analyzed using traditional techniques. The overall response of the ionosphere is presented and compared with previous measurements and recent predictions.

Key Points:
- High-resolution observations were made using two VIPIR ionosondes
- Simultaneous vertical and oblique incidence ionosphere soundings were analyzed
- Increase in *F*2 layer peak height is not consistent with predicted downward ion flow

Correspondence to:
T. Bullett,
terry.bullett@noaa.gov

Citation:
Bullett, T., & Mabie, J. (2018). Vertical and oblique ionosphere sounding during the 21 August 2017 solar eclipse. *Geophysical Research Letters*, *45*, 3690–3697. https://doi.org/10.1002/2018GL077413

Received 31 JAN 2018
Accepted 20 MAR 2018
Accepted article online 26 MAR 2018
Published online 16 APR 2018

1. Introduction

Solar eclipses provide the opportunity to observe natural ionosphere plasma processes under unusual but relatively controlled conditions. Types of phenomenon that can be probed during an eclipse include changes in *E* and *F* region height and plasma densities (Chen et al., 2015), winds launched toward the center of totality (Risbeth, 1963) and waves launched along the eclipse path (Adams et al., 2010), vertical plasma motions driven by neutral winds (Boitman et al., 1997) and changes in vertical plasma density profiles (Chen et al., 2015), D region absorption (Singh et al., 2011), composition and chemistry changes in the thermosphere (Adams et al., 2010), and the accuracy of global ionosphere/thermosphere models (Muller-Wodarg & Aylward, 1998).

The primary mechanisms of eclipse induced ionosphere forcing can be explained through simple occultation of solar radiation. The physics are well understood and can be modeled by applying Beers law to the incident spectrum of solar radiation onto the atmospheric profile (Boitman et al., 1997; Chen et al., 2015). It is the response of the thermosphere and coupling to the ionosphere which can be complex (Chen et al., 2015).

There have been many observations of the response of the ionosphere to solar eclipses. These investigations have found that the response of the *E* and *F*1 layers are primarily the result of photochemical processes (Muller-Wodarg & Aylward, 1998), and the response of the F2 layer can be dominated by transport (Chen et al., 2011; Zhang et al., 2017). Eclipse-induced waves in the ionosphere can be observed by the resulting plasma displacements (Negrea, 2016) and can be generated by photochemistry (Adams et al., 2010) or changes in temperature (Zhang et al., 2017).

2. Previous Results

Solar eclipses have been attributed to increases in the height of the ionospheric D and F2 layers (Chen et al., 2015). Increases in hmF2 have been attributed to different rates of recombination at different altitudes due to

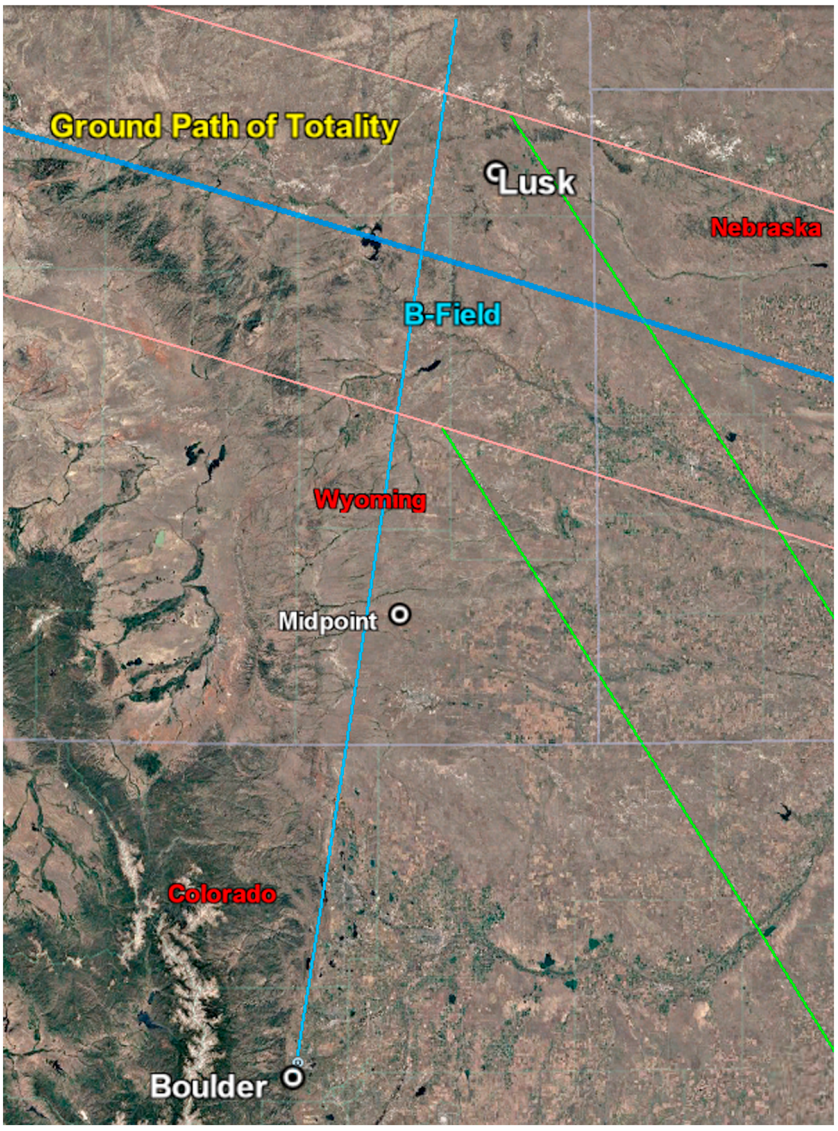

Figure 1. Map of the observation region showing the center of totality (light blue line), boundary of totality (red line), the geomagnetic field orientation (dark blue line), and the location of the two Vertical Incident Pulsed Ionospheric Radar systems. The great circle path is shown as a white line. The horizontal projection of the path of totality at 17:47 UT is shown as two green lines.

differences in time constants, atmospheric constituents, densities, and vertical plasma transport. Typical changes in hmF2 have been found to be on the order of 20 km (Boitman et al., 1997; Le et al., 2009). During a solar eclipse, the density of the *F*1 layer decreases reaching a minimum near totality and increases after (Cheng et al., 1987). The peak density of the F2 layer has been observed to be delayed and can either increase or decrease. Generally, the neutral atmosphere density near hmF2 is much lower than near hmF1 resulting in longer time constants for chemical processes and temperature fluctuations. The delay in the F2 response is typically around 30 min (Boitman et al., 1997; Buonsanto, 1999; Muller-Wodarg & Aylward, 1998) but can vary from a few minutes to more than an hour (Chen et al., 2011) and increases with altitude (Risbeth, 1963).

The direct effects of the eclipse on foF2 include thermal increase in NmF2 due to atmospheric drop in temperature and a competing chemical decrease in foF2 due to a decrease on the concentration of molecular nitrogen (Muller-Wodarg & Aylward, 1998). The indirect effects on foF2 can be more significant including a

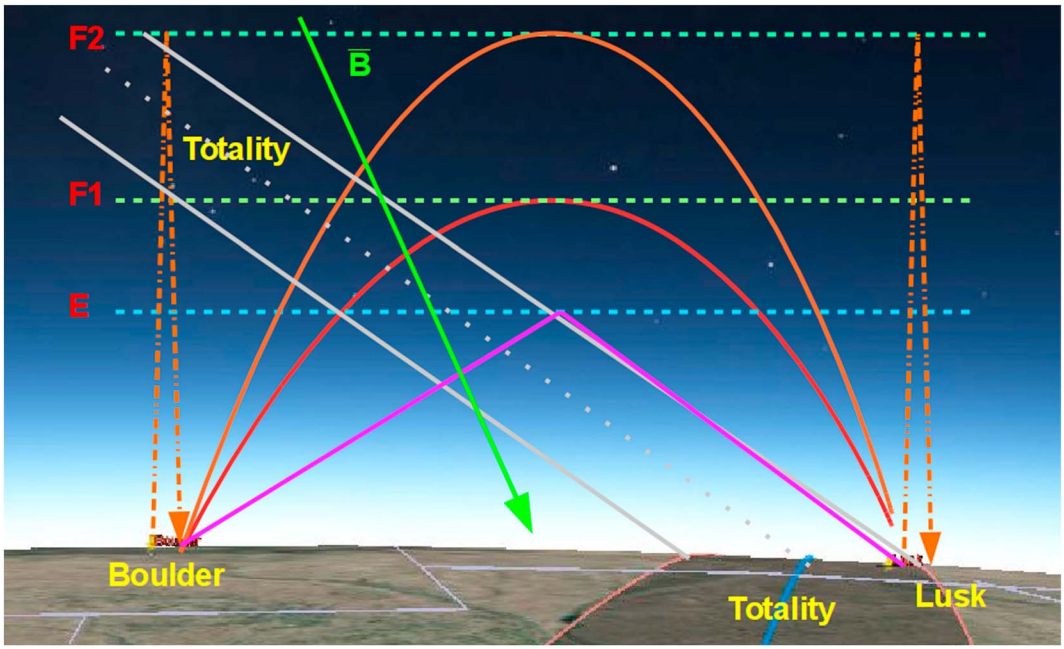

Figure 2. Representation of the observation geometry showing the location of the two Vertical Incident Pulsed Ionospheric Radar systems with respect to the path of totality including the vertical orientation (gray lines are boundary of totality), the paths of vertical incidence propagation (orange), the approximate altitudes of the *E* layer peak (blue dash) and *F* layer peaks (green dash), and the OI propagation paths in the *F*1 and *F*2 layers (purple and red). The magnetic field dip of 66° is a green arrow. The Lusk, WY, vertical incidence observations are north of totality in the ionosphere; the Boulder, CO, observations are south of totality in the ionosphere; and the OI observations from both sites are within totality in the ionosphere.

twofold increase in NmF2 due to downward plasma transport from the plasmasphere (Boitman et al., 1997; Chen et al., 2011).

Neutral atmosphere waves are known to be caused by solar eclipses. The Vertical Incident Pulsed Ionospheric Radar (VIPIR) ionosonde is capable of resolving wave activity by producing high signal-to-noise ratio observations that include Doppler shifts and wave vectors through interferometry. The Dynasonde analysis approach produces plasma velocity and ionospheric tilt values from these observations (Zabotin et al., 2006). There is some disagreement on the source of eclipse-induced gravity waves. Earlier investigation suggested that these waves were launched by thermal cooling in the ozone layer (Zhang et al., 2017), but more recent work suggests that they may be launched from changes in the photoionizaton rate in the ionosphere between the *F*1 and *F*2 regions (Chen et al., 2015).

3. Experiment

This solar eclipse provided a unique geometry to study vertical and short path oblique ionospheric sounding during the event. The path of totality was approximately orthogonal to the magnetic meridian at the permanent ionosonde station in Boulder, Colorado (39.992°N 105.269°W) (Bullett, 2008; Grubb et al., 2008). Resources available allowed for the deployment of one VIPIR instrument on loan from the U.S. Naval Research Laboratory. A temporary field site was established within the path of totality in Lusk, Wyoming (42.750°N, 104.455°W), providing a ground path distance of 313 km at a bearing 12°W, which is nearly parallel to the geomagnetic field line declination of 8°W. The Lusk field site was 40 km NE of the Boulder magnetic field line and the eclipse centerline. Figure 1 shows the experimental configuration. The intent of this geometry was to measure the eclipse-induced dynamics in this magnetic meridian (Adams et al., 2010). A midday eclipse also helps simplify the analysis because it is away from the day-night terminator which causes an atmospheric response similar to the eclipse itself (Singh et al., 2011).

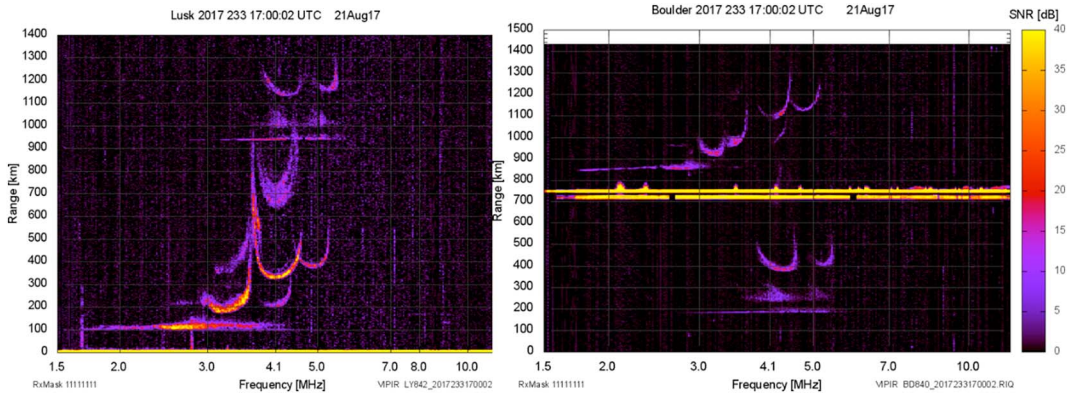

Figure 3. Global Positioning System-disciplined phase-locked simultaneous observations of vertical incidence and oblique incidence ionograms from Boulder, CO (right) and Lusk, WY (left) at 17:00UT, about 1 hr into the eclipse. Transmissions from Boulder are delayed by 5 ms and are observed as high amplitude signals at 750 km range along with transmissions from the colocated Boulder Digisonde sharing the transmitter. The VI observations begin around 750 km range in Boulder and 0 km range in Lusk while the OI observations begin at 0 km in Boulder and around 750 km in Lusk. VIPIR = Vertical Incident Pulsed Ionospheric Radar; SNR = signal-to-noise ratio.

The notional propagation geometry along the great circle path is shown in Figure 2. Because of the solar angle at totality of 55° elevation, 147° azimuth and the eclipse ionosphere shadow being approximately a cylinder, the Lusk vertical incidence (VI) ionosphere observations are made outside the region of totality, whereas Boulder VI measurements are closer to totality. The oblique incidence (OI) observations are close to totality for the *E* layer and increasingly away from totality with ionosphere altitude.

4. Observations

The Boulder VIPIR was calibrated and operated continuously starting 1 week prior to the eclipse. The Lusk VIPIR was deployed, calibrated, and operated continuously for 1 day prior and 2 days post eclipse. Both instruments were operated in a Dynasonde B-mode (Wright & Pitteway, 1994) sweep frequency from 1,500 to 12,000 kHz with a logarithmic step of 0.7%. The interpulse period was limited to 10 ms to allow synchronized operation with the operational Boulder Digisonde. The measurement time was 96 s, and measurements were

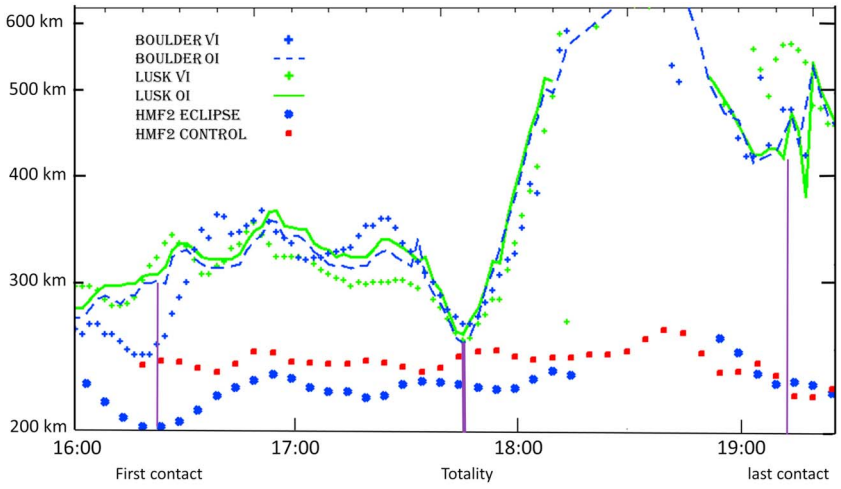

Figure 4. Virtual heights h′F2 for the *F*2 layer from Boulder and Lusk, vertical incidence (VI) and oblique incidence (OI) for *E*, *F*1, and *F*2 layers. The crosses are vertical incidence observations. The blue dashed line is Boulder ➔ Lusk OI and the green line is Lusk ➔ Boulder OI. True *F*2 layer peak heights hmF2 from the Boulder Digisonde are shown for the eclipse (blue dots) and for the day after (red squares) as a control. *F*2 layer virtual heights between 18:10 and 19:00 are during the *G* condition and no hmF2 can be observed at these times.

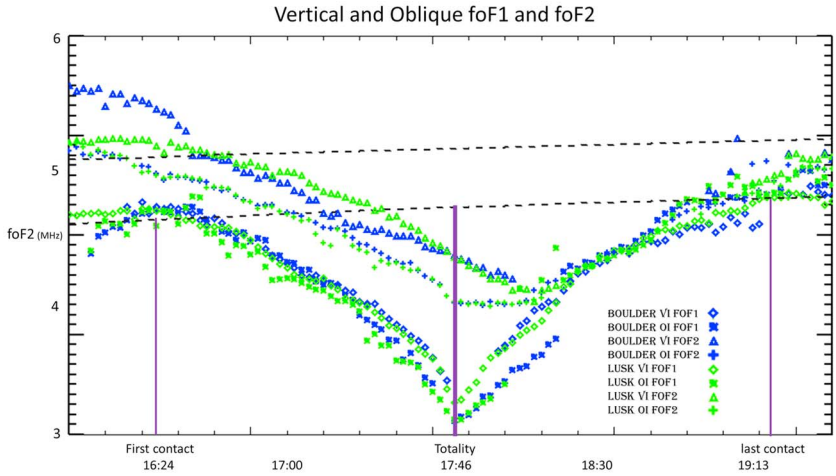

Figure 5. Manually scaled vertical incidence (VI) values of foF1 and foF2 for Boulder and Lusk, and equivalent vertical foF1 and foF2 values at the midpoint obtained from oblique incidence (OI) propagation received at Boulder and Lusk. Control data for the previous day vertical incidence foF1 and foF2 are fit to a polynomial and displayed as dashed lines.

repeated every 2 min. Both instruments were synchronized to Global Positioning System (GPS) time and incorporated a GPS disciplined 10 MHz rubidium oscillator to maintain a long-term frequency stability of about 1 cycle per day, allowing measurement of the oblique group and phase paths with negligible instrumentation bias.

Since both Boulder and Lusk were operating on precisely the same time-frequency pattern, and given the relatively short (313 km) ground path, oblique and vertical echoes were often overlapped in range. While in theory these could be separated in arrival angle space, the VIPIR design allows the placement of the transmit pulse anywhere within the radar's interpulse period. The transmit pulse of the Boulder VIPIR was shifted to 5 ms, and the effects of this are shown in Figure 3. For Lusk, the bottom half of the ionogram are VI echoes only, while the top half can be long range VI and OI echoes from Boulder. For Boulder, the bottom half of the ionogram has OI echoes from Lusk and the top half has VI echoes from Boulder. This allows unambiguous separation of OI and VI echoes from both instruments simultaneously and is a unique feature of this experiment.

The times of first contact (16:25 UT), totality (17:46–17:48 UT), and last contact (19:13 UT) are shown on Figures 4 and 5 are for the ground at Lusk. These times are within 2 min for all locations below the ionosphere F2 peak for the entire experimental volume shown in Figures 1 and 2. This is also the time resolution of the data.

5. Results

In this investigation, signal-to-noise ratio plots of echo signal strength as a function of time and frequency, as in Figure 3, are scaled manually to produce values of virtual heights and critical frequencies of the *E*, *F*1, and *F*2 layers for both VI and OI observations, every 2 min from 16:00 to 19:30 UT (10:00–13:30 local time). Persistent sporadic-*E* made direct observations of the *E* layer densities problematic. Corrections are made for the transmit time delays in the Boulder data. Identification of critical heights and frequencies in the traces was performed using international standards of hand scaling of ionograms (Piggott & Rawer, 1972).

The scaled Lusk VI, Boulder VI, corrected Lusk ➔ Boulder OI and corrected Boulder ➔ Lusk OI values of virtual F2 layer heights are plotted in Figure 4. For OI observations it is necessary to compute equivalent virtual height at the oblique midpoint using Martyn's Equivalent Path theorem (Davies, 1969)

$$P(f) = h'(f) \times \sec(\varphi) \tag{1}$$

where $P(f)$ is the virtual path length, φ is the ionosphere entry angle, $h'(f)$ is the equivalent virtual height, and the dependent variable f is frequency. The virtual path length was computed by time of flight of the radio

wave assuming a single ionospheric reflection at the midpoint, noting that this assumes horizontal stratification along the propagation path and is a source of uncertainty.

The *E* layer virtual height data are largely from the persistent sporadic-*E* layer and show no discernible change during the eclipse. The close agreement between all four measurements indicate spatial uniformity in the height of the Es layer. Similarly for the *F*1 layer, there is larger spread in the four observations, but all observations are nominally 180 km for the duration. Figure 4 also shows peak F2 layer height for the eclipse day and the following day as a reference. These data were obtained from the Boulder Digisonde ionograms every 5 min, using manual ionogram virtual height trace recognition and NHPC inversion for electron density profile true heights and hmF2 (Huang & Reinisch, 1996), with a three-point binomial smoothing operator applied. The F2 layer data show significant eclipse effects, and some differences between the observation locations. Prior to first contact, there is a height decrease in Lusk h′F2 and Boulder Digisonde hmF2, but not in Boulder VIPIR h′F, due to a traveling ionospheric disturbance. At first contact, the Lusk h′F values and Boulder hmF2 values increase. The Boulder hmF2 values remain 15 to 20 km below the reference day values through totality but are rising to meet the control day values when the *G* condition hits at 18:05 UT, and it is not possible for Boulder Digisonde to measure hmF2. When the *G* condition ends at 19:10, the hmF2 has already returned to the control day values. Prior to totality, there is a sudden drop in F2 layer virtual heights to 250 km and a rapid rise after totality, until 600 km when the F2 layer enters the *G* condition at 18:10 UT and the h′F2 data become intermittent. This had very little influence on the hmF2 value. Occasional values of h′F2 from the Lusk ➔ Boulder OI and Boulder VI suggest the h′F2 during the *G* condition is between 600 and 700 km and starting to descend around 18:45 UT. When the F2 layer reappears around 19:00 UT, the h′F2 virtual height is some 100 km higher at Lusk than at Boulder and both observations of the midpoint. After last contact, the observed layer heights converge on 450 km. The real peak height of the layer rises steadily by 25 km between first contact and last contact then rapidly drops to the reference day value within 30 min after last contact.

Vertical incidence critical frequency values of foF1 and foF2 were manually scaled from the Boulder and Lusk VI ionograms, and oblique maximum observed frequencies were manually scaled for the *F*1 and *F*2 traces in the OI ionograms. The observed OI frequencies were converted into equivalent vertical frequencies at the midpoint using the relationship (Davies, 1969):

$$f_{\mathrm{obs}} = f_{\mathrm{VI}} \times \sec(\varphi) \tag{2}$$

where f_{obs} is the observed critical frequency and f_{VI} is the equivalent VI frequency. For this calculation, the ionospheric entry angle φ is computed from the measured arrival angle of the received OI echo using phase interferometry across the receive array at Lusk. Boulder arrival angle data have an unresolved phase calibration issue and are not used. The VI and equivalent VI values are plotted in Figure 5 for foF1 and foF2. Also shown are control values from the previous day, shown as a polynomial fit to manually scaled values. The foF1 data show a clear and direct relationship to the solar occultation, with eclipse day values departing from the control value just after first contact, minimizing at totality, and restoring to control day values at last contact. Boulder and Lusk VI foF1 values are nearly identical for the entire eclipse. The inflection in the foF1 data near 18:10 UT approximately correlate with the reemergence of the large sunspot region and could be an ionospheric response to changes in solar radiation.

The OI foF1 values are slightly lower but very similar to each other, as they represent oblique propagation through the same ionosphere but in different directions. The offset of 5% between the VI and OI data are likely due to differences in the simple correction model and the actual propagation conditions. The foF2 data in Figure 5 show a markedly different response. Boulder VI foF2 starts high compared to the control day, but quickly drops to the Lusk and control values after first contact. The VI foF2 values largely track each other, dropping more slowly than foF1 and to a minimum value of 3.5 MHz at 18:10 UT, when the F2 density starts to slowly increase just as the rapid foF1 increase exceeds foF2. The OI midpoint values of foF2 are also consistently below the VI values, again likely due to the simple propagation model used to compute the equivalent vertical values. The midpoint foF2 reaches a minimum value just at totality, stays constant for 20 min then starts to increase closer to 18:00 UT.

A very important detail in Figure 5 are the Lusk ➔ Boulder OI observations of the midpoint foF2 during the *G* condition 18:10–19:00 UT. Normally, it is not possible to observe foF2 with an ionosonde under the *G* condition, for when foF2 $<$ foF1. However, in this oblique incidence geometry, and only for the Lusk ➔ Boulder

propagation direction, there were several ionograms where the F2 layer was observed above the *F*1 layer. This necessarily violates the assumption of horizontal stratification required by the simple propagation model used but did allow occasional measurement of h'F2 and foF2 between 18:10 and 19:00.

6. Discussion

Variations in the *E* and *F*1 layer heights during an eclipse have been attributed mostly to photochemistry while the F2 layer variations are attributed mostly to transport (Le et al., 2009). During totality, the foF1 dropped to 2.1 MHz or an electron density of 0.54×10^{11} (m^{-3}) compared to the control day value of 4.2 MHz or 2.2×10^{11} (m^{-3}), a change of −75%, and the loss and restoration of the plasma follow the solar illumination pattern closely. The VI observed values of foF2 dropped to a low value of 3.5 MHz plasma frequency or 1.5×10^{11} (m^{-3}) electron density, compared to a control day value of 4.9 MHz or 3.0×10^{11} (m^{-3}), a depletion of −50%. The true *F*2 layer peak height increased from 220 km at first contact to 250 km at last contact. The predictions of *F*2 density change for midlatitudes by Le et al. (2009) are also a −50%, and the predicted hmF2 change of +20 km is consistent with the observed +25 km change but is inconsistent with the SAMI3 predictions of Huba and Drob (2017), which predict a −20 (m/s) *F* region plasma velocity along the magnetic field line during the eclipse. The nature of virtual height during a near *G* condition indicates a change in the electron density profile with a vertical redistribution of plasma. Future full electron density profile analysis will provide quantitative values to compare with the detailed SAMI3 ionosphere predictions.

The density of the neutral atmosphere is much larger at 140 km near the *F*1 peak than it is at 220 km near the *F*2 peak; the rate of recombination is much greater in the *F*1 region (Buonsanto, 1999). The response of the *F*1 layer occurs more rapidly and reaches a minimum density within a minute of totality. The *F*2 response is much slower and delayed 30 min consistent with previous investigations (Boitman et al., 1997; Chen et al., 2011; Muller-Wodarg & Aylward, 1998). This results in foF1 becoming larger than foF2 for about 50 min. It is noted that net plasma loss leading up to totality and net plasma production during recovery follow very different but distinct curves. The hmF2 true height changes suggest that this a change in plasma transport and the large change in virtual height suggest significant changes to the electron density profile.

7. Summary

Two GPS-disciplined phase-locked VIPIR ionosondes were used to make unique, high-resolution, simultaneous vertical and oblique soundings of the ionosphere during the total solar eclipse on 21 August 2017, along a magnetic meridian perpendicular to the path of totality. Initial analysis using hand scaling of ionograms and a simple propagation model show that these observations are consistent with many previous observations and also include new observations including increases in *F* layer heights and oblique observations of the *F*2 layer during the *G* condition. Model predictions of downward ionization flow need to be reconciled with the observed increase in *F* layer peak heights using full electron density profile analysis and Doppler velocity calculations.

Acknowledgments
Travel support was provided by Virgina Technical University under grant 479505-19557; the U.S. Naval Research Laboratory provided the bistatic VIPIR. The Town of Lusk, WY, provided logistics support; Kevin Knott from NOAA/ESRL fabricated antenna parts.

References

Adams, C., McLinden, C. A., Strong, K., & Umlenski, V. (2010). Ozone and NO_2 variations measured during the 1 August 2008 solar eclipse above Eureka, Canada with a UV-visible spectrometer. *Journal of Geophysical Research*, *115*, S19310. https://doi.org/10.1029/2010JD014424

Boitman, O. N., Kalikhman, A. D., & Tashchilin, A. V. (1997). The midlatitude ionosphere during the total solar eclipse of March 9. *Journal of Geophysical Research*, *104*(A12), 28,197–28,206. https://doi.org/10.1029/1999JA900228

Bullett, T. (2008). Station report: A new ionsonde at Boulder, INAG v.69.

Buonsanto, M. J. (1999). Ionospheric storms—A review. *Space Science Reviews*, *88*(3/4), 563–601. https://doi.org/10.1023/A:1005107532631

Chen, G., Wu, C., Huang, X., Zhao, Z., Zhong, D., Qi, H., et al. (2015). Plasma flux and gravity waves in the midlatitude ionosphere during the solar eclipse of 20 May 2012. *Journal of Geophysical Research: Space Physics*, *120*, 3009–3020. https://doi.org/10.1002/2014JA020849

Chen, G., Zhao, Z., Ning, B., Deng, Z., Yang, G., Xhou, C., et al. (2011). Latitudinal dependence of the ionospheric response to solar eclipse of 15 January 2010. *Journal of Geophysical Research*, *116*, A06301. https://doi.org/10.1029/2010JA016305

Cheng, K., Huang, Y., & Chen, S. (1987). Ionospheric effects of the solar eclipse of September 23, around the equatorial anomaly crest region.

Davies, K. (1969). Ionospheric radio waves. *Ionospheric radio waves., by Davies, K.. Blaisdell, MA (USA), 17+ 460 p.*

Grubb, R. N., Livingston, R., & Bullett, T. W. (2008). A new general purpose high performance HF Radar. *XXIX URSI General Assembly*.

Huang, X., & Reinisch, B. W. (1996). Vertical electron density profiles from the digisonde network. *Advances in Space Research*, *18*(6), 121–129. https://doi.org/10.1016/0273-1177(95)00912-4

Huba, J. D., & Drob, D. (2017). SAMI3 prediction of the impact of the August 21, 2017 total solar eclipse on the ionosphere/plasmasphere system. *Geophysical Research Letters*, *44*, 5928–5935. https://doi.org/10.1002/2017GL073549

Le, H., Liu, L., Yue, X., Wan, W., & Ning, B. (2009). Latitudinal dependence of the ionospheric response to solar eclipses. *Journal of Geophysical Research*, *114*, A07308. https://doi.org/10.1029/200JA014072

Muller-Wodarg, I. C. F., & Aylward, A. D. (1998). Effects of a mid-latitude solar eclipse on the thermosphere and ionosphere—A modelling study. *Geophysical Research Letters*, *25*(20), 3787–3790. https://doi.org/10.1029/1998GL900045

Negrea, C. (2016). Characteristics, variability and impact of atmospheric gravity waves in the thermosphere-ionosphere as determined from dynasonde data. Electrical Engineering Graduate Theses & Dissertations. 15. Retrieved from https://scholar.colorado.edu/eeng_gradetds/15

Piggott, W. R., & Rawer, K. (1972). *URSI handbook of ionogram interpretation and reduction, UAG-23A*.

Risbeth, H. (1963). Further analogue studies of the ionospheric F layer. *Proceedings of the Physical Society*, *81*(1), 65–77. https://doi.org/10.1088/0370-1328/81/1/312

Singh, R., Veenadhari, B., Maurya, A. K., Cohen, M. B., Kumar, S., Selvakumaran, R., et al. (2011). D-region ionosphere response to the total solar eclipse of 22 July 2009 deduced from ELF-VLF tweek observations in the Indian sector. *Journal of Geophysical Research*, *116*, A10301. https://doi.org/10.1029/2011JA016641

Wright, J. W., & Pitteway, M. L. V. (1994). High-resolution vector velocity determinations from the dynasonde. *Journal of Atmospheric and Terrestrial Physics*, *56*(8), 961–977. https://doi.org/10.1016/0021-9169(94)90157-0

Zabotin, N. A., Wright, J. W., & Zhbankov, G. A. (2006). NeXtYZ: Three-dimensional electron density inversion for dynasonde ionograms. *Radio Science*, *41*, RS6S32. https://doi.org/10.1029/2005RS003352

Zhang, S.-R., Erickson, P. J., Goncharenko, L. P., Coster, A. J., Rideout, W., & Vierinen, J. (2017). Ionospheric bow waves and perturbations induced by the 21 August 2017 solar eclipse. *Geophysical Research Letters*, *44*, 12,067–12,073. https://doi.org/10.1002/2017GL076054